Thermoelectric properties of the stripe-charge ordering phases in IrTe₂

Jung Sang You [1,2] Man Jin Eom,[2] Minhyea Lee [3] Y. J. Jo,[4] C. J. Won [5,6]

S.-W. Cheong,[5,7] Kyoo Kim,[2,6,8,*] and Jun Sung Kim[1,2,†]

[1]*Center for Artificial Low Dimensional Electronic Systems, Institute for Basic Science, Pohang 37673, Korea*

[2]*Department of Physics, Pohang University of Science and Technology, Pohang 37673, Korea*

[3]*Department of Physics, University of Colorado, Boulder, Colorado 80309, USA*

[4]*Department of Physics, Kyungpook National University, Daegu 41566, Korea*

[5]*Laboratory for Pohang Emergent Materials, Pohang Accelerator Laboratory, Pohang 37673, Korea*

[6]*MPPC-CPM, Max Planck POSTECH/Korea Research Initiative, Pohang 37673, Korea*

[7]*Rutgers Center for Emergent Materials and Department of Physics and Astronomy,*

Rutgers University, Piscataway, New Jersey 08854, USA

[8]*Korea Atomic Energy Research Institute, 111 Daedeok-daero 989 Beon-Gil, Yuseong-gu, Daejeon 34057, Korea*

We investigate the effects of stripe-charge ordering on the thermoelectric power of IrTe₂, together with other transport properties, including the resistivity, thermal conductivity, and Hall effect. At the stripe-charge ordering transitions, clear transport anomalies such as abrupt changes in the thermoelectric power and Hall effect are observed and attributed to multiband conduction due to stripe-order-driven Fermi surface (FS) reconstruction. This FS reconstruction depends sensitively on intralayer charge modulations and interlayer staircaselike arrangements, leading to complex sign changes in the thermoelectric power. These results are in good agreement with the Boltzmann transport calculations based on the reconstructed FS and confirm the strong impact of the stripe charge order on the intrinsic charge conduction in IrTe₂.

I. INTRODUCTION

Transition metal dichalcogenides (TMDCs) host various kinds of electronic phases owing to an interplay between charge, orbital, and lattice degrees of freedom [1–9]. The most commonly observed electronic phase in TMDCs is the charge density wave (CDW) phase with spontaneous periodic charge modulations. These CDW phases have different periods and patterns, depending on Fermi surface (FS) nesting and electron-phonon coupling [1,3,8], which are sometimes accompanied by Mott or excitonic insulating phases (e.g., in $1T$-TaS₂ and TiSe₂) [4,5]. Recently, another intriguing charge ordered phase was discovered in IrTe₂ with the same crystal structure as $1T$-type TMDCs [10–16]. This charge ordering transition in IrTe₂ is associated with stripe-type intralayer Ir-Ir dimerization and interlayer Te-Te polymerization, which does not exhibit the common features of the CDW transition such as a partial CDW gap opening at the FS [12,17,18] and phonon softening [15]. Instead, charge disproportionation on the Ir sites occurs without loss of metallicity [14,19,20], and superconductivity is induced when this charge order is suppressed by doping [10–13,21–23]. Because of these unique properties, IrTe₂ provides a rare opportunity for studying the charge ordering phenomena in the metallic state and their impact on superconductivity.

The stripe-charge order of IrTe₂ is highly sensitive to doping or strain in the crystal and yields different modulation patterns with periods of $5a_0$, $6a_0$, and $8a_0$, where a_0 is the in-plane lattice constant in the high-temperature hexagonal phase [10–17,19–33]. This diversity suggests that several instabilities with different charge modulations compete with each other in IrTe₂. The interlayer configuration, however, is common in these phases and resemble staircases, as shown in Fig. 1, which significantly affects the electronic properties of IrTe₂. In particular, the density of states (DOS) is expected to be suppressed in the planes of Ir-Ir dimers running across the IrTe₂ layers. These peculiar charge patterns may result in cross-layer quasi-two-dimensional states, which exhibit dominant charge conduction along the interlayer staircaselike patterns rather than along the layered crystal structure. The existence of this intriguing metallic state, predicted by theoretical calculations [16,31,34], was indirectly confirmed by de Haas–van Alphen (dHvA) oscillations [26,27]. However, the effects of the stripe-charge order on the electrical conduction has not been thoroughly investigated because its experimental signature is masked by the complex domain formation and strong scattering at the domain boundaries.

In this work, we address this issue by investigating the thermoelectric power S of high-quality IrTe₂ crystals. Unlike the electrical or thermal conductivities, the thermoelectric power is less sensitive to domain boundary scattering and thus more suitable for investigating the intrinsic effect of the stripe-charge order. We observed the complex sign changes in $S(T)$ across the transitions, which cannot be understood in

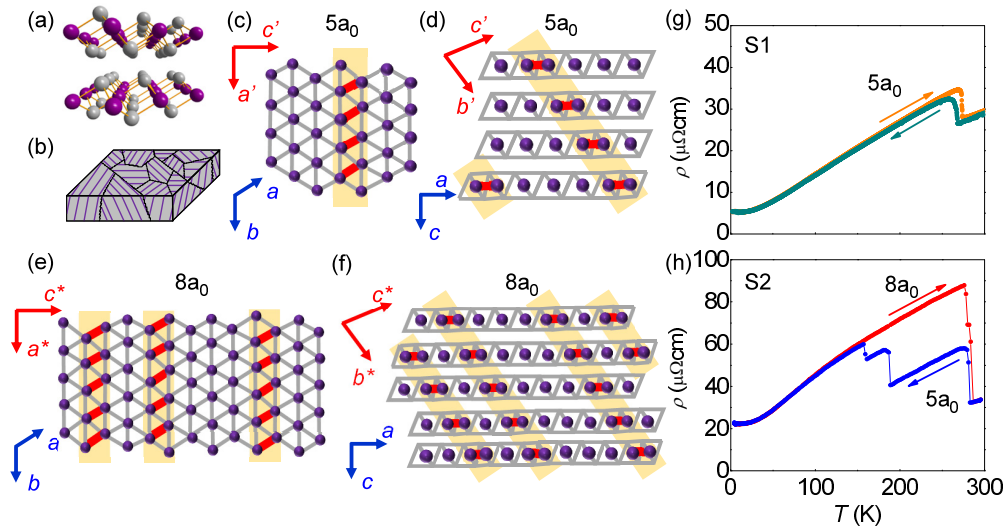*kyoo@kaeri.re.kr

†js.kim@postech.ac.kr

FIG. 1. (a) Crystal structures of IrTe$_2$ in the high-temperature normal phase. (b) Schematic illustration of domain formation of three different orientations. Ir atoms in unit cells of two stripe-charge ordering phases are presented in (c) and (d) 5a_0 and (e) and (f) 8a_0. Resistivities of (g) S1 and (h) S2 during cooling and warming, as indicated with arrows.

terms of the dominant carrier type, identified by the Hall effect measurements. Instead, by considering FS reconstruction due to the stripe-charge order, such behaviors can be well reproduced with Boltzmann transport calculations. Our results, therefore, provide experimental evidence for the FS reconstruction and presence of the cross-layer two-dimensional state in the charge ordered phases in IrTe$_2$.

II. METHODS

Single crystals of IrTe$_2$ were grown in a vacuum-sealed quartz ampule with the Te-flux method (Ir:Te = 1:4). We obtained two types of crystals by applying different cooling methods. Sample 1 (S1) was quenched from 950 °C to the room temperature, and sample 2 (S2) was slowly cooled to room temperature at a rate of 5 °C/h. [26] X-ray diffraction and energy dispersive spectroscopy results confirm that these two samples have nearly the same crystallinities and stoichiometries within the experimental resolution. The resistivity ρ, thermoelectric power S, thermal conductivity κ, and Hall resistivity ρ_{xy} were measured in a 14-T physical property measurement system (Quantum Design). The directions of the applied electric current and temperature gradient were along the b axis of the normal phase, and the amplitude of temperature gradient was less than 3% of the sample temperature for the thermoelectric power measurements. For the Hall measurements, we used the conventional six-probe method with the applied magnetic field perpendicular to the crystal plane. For the band structure calculations, we used the full-potential local orbital (FPLO) method, implemented in FPLO code, in a fully relativistic way within the Perdew-Burke-Ernzerhof exchange-correlation functional [35], as described in Refs. [26,32]. Particularly, we calculated Fermi velocity on each FS for the different stripe-charge ordering phases, which was important for Boltzmann transport calculation, using Boltzmann [36] code implemented in WANNIER90 [37].

III. RESULTS AND DISCUSSION

The resistivity ρ of the quenched (S1) and slowly cooled (S2) crystals exhibits metallic temperature dependence and clear resistive transitions [Figs. 1(g)) and 1(h)], consistent with previous reports [10–14,19,21–26]. For S1, the resistive transitions occur near $T_1 \sim 270$ K with a small thermal hysteresis [Fig. 1(g)]. However, S2 undergoes two successive transitions at $T_1 \sim 280$ K and $T_2 \sim 180$ K during cooling and one transition during warming at $T_1 \sim 280$ K [Fig. 1(h)]. These first-order transitions with significant thermal hysteresis are attributed to the formation of a stripe-charge ordering with different periods, 5a_0 [Figs. 1(c) and 1(d)] and 8a_0 [Figs. 1(e) and 1(f)]. The stripe-charge ordering phases include two kinds of Ir ions. One forms Ir-Ir dimers and has a relatively high valence, closer to Ir^{4+} and denoted as "4." The other has a relatively low valence, closer to Ir^{3+} and denoted as "3." The 5a_0 phase corresponds to a pattern of Ir atoms with sequences of 33344. Similarly, the 8a_0 phase mainly exhibits the charge order sequence 33344344 with a minority phase of 34444344 [19]. The detailed patterns and periods of the charge order are known to be sensitive to the defect density and internal strain in IrTe$_2$ crystals [19,26]. Thus, S1 and S2 crystals, grown with different cooling procedures, exhibit different phase transitions.

Recent scanning tunneling spectroscopy measurements on IrTe$_2$ revealed the existence of twin domains in the stripe phases of IrTe$_2$ [20,25,33]. The stripe dimer patterns can be oriented along three equivalent directions in the high-temperature hexagonal lattice, and there are three different domains, rotated by 120° with respect to each other. Therefore, charge conduction along the stripe direction within one domain is interrupted at the boundaries that face the neighboring domains [Fig. 1(b)]. Consequently, charge conduction is dominated by strong scattering at the domain boundaries, rather than by intrinsic conduction within the domain. For comparison, we calculated the resistivities of the
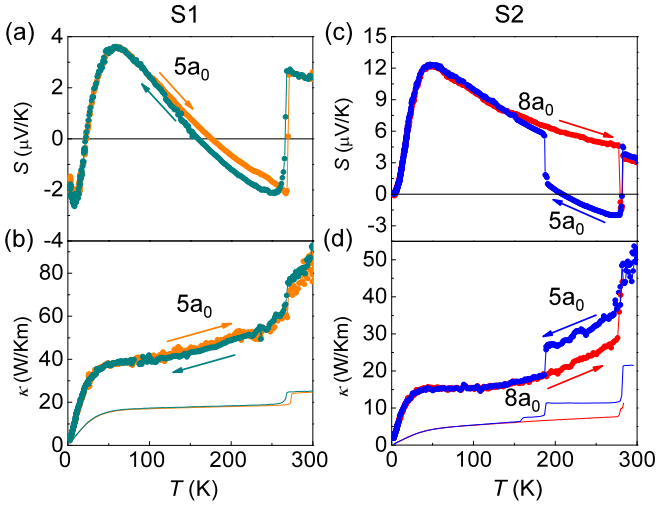
FIG. 2. Temperature-dependent thermoelectric power $S(T)$ (a), (c) and thermal conductivity $\kappa(T)$ (b), (d). Data from S1 and S2 correspond to (a), (b) and (c), (d), respectively. Arrows and symbol-colors indicate the direction of temperature sweep. The electron contributions of thermal conductivity, estimated from Wiedermann-Franz law, are plotted (thin solid lines) for S1(b) and S2(d).

high-temperature normal and the low-temperature stripe ($5a_0$ and $8a_0$) phases using the Boltzmann transport method. The jump in the resistivity is expected to be $\sim 120\%$ from the normal phase to the $5a_0$ phase and $\sim 15\%$ from the $5a_0$ phase to the $8a_0$ phase. Clearly, this calculation cannot reproduce the much larger resistive jump observed in experiments [Figs. 1(g) and 1(h)]. These results indicate the significant contribution of the domain boundary scattering to the observed abrupt increase in the resistivity at the transition temperatures.

The stripe-charge order also affects the thermal transport properties such as the thermoelectric power and thermal conductivity. Both S1 and S2 show clear anomalies in the temperature-dependent thermoelectric power $S(T)$ and thermal conductivity $\kappa(T)$ at the transition temperatures, T_1 and T_2 (Fig. 2), consistent with the resistivity results [Figs. 1(g) and 1(h)]. With decreasing temperature, $\kappa(T)$ drops at each transition temperature. The decrease in $\kappa(T)$ at T_1 is comparable to that of the electronic contribution $\kappa_e(T)$, estimated with the Wiedemann-Franz law $\kappa_e(T) = LT/\rho(T)$, where the Lorentz number $L = \frac{\pi^2}{3}(\frac{k_B}{e})^2$ [38]. Therefore, the decrease in $\kappa(T)$ at the transition temperatures is mainly due to the reduction in the electrical conductivity, caused by strong domain boundary scattering.

The thermoelectric power $S(T)$ shows a complicated temperature dependence. At low temperatures, both samples exhibit a broad $S(T)$ peak at $T^* \sim 50\,\mathrm{K}$. The broad peak can be attributed to the phonon drag effect, which induces a characteristic peak in $S(T)$ at $T^* \sim \theta_D/5$, where θ_D is the Debye temperature ($\theta_D \sim 210\,\mathrm{K}$ for IrTe$_2$) [11,23,24]. Below T^*, $S(T)$ of S2 monotonically approaches zero, in accordance with the Mott relationship [39], $S = \frac{\pi^2 k_B^2 T}{3e} \frac{N(\epsilon_F)}{n}$, where $N(\epsilon_F)$ is the DOS at the Fermi level and n is the carrier density. However, S1 shows an additional sign change, which may be related to multiband conduction with nontrivial electron scattering. More importantly, at the transition temperatures,

$S(T)$ of S1 and S2 exhibits abrupt sign changes [Figs. 2(a) and 2(c)]. In the normal phase, $S(T)$ is positive, which is consistent with the hole-type electronic structure, according to the band-structure calculations and angle-resolved photoemission spectroscopy (ARPES) results [19,31,32,40]. Once the system enters the $5a_0$ phase below T_1, $S(T)$ drops suddenly to a negative value in both samples. However, $S(T)$ of S2 abruptly jumps to a positive value at T_2 during the $8a_0$ phase transition. Unlike those of the electrical and thermal conductivities, the changes in $S(T)$ at the transition temperatures T_1 and T_2 are in opposite directions, which cannot be explained with domain boundary scattering.

Such sign changes in $S(T)$ are usually considered a signature of multiband conduction. Being a zero-current property, $S(T)$ is much less sensitive to domain boundary scattering than the electrical conductivity. Band structure calculations [26] indicate that $5a_0$- or $8a_0$-type charge orders induce the reconstruction of electronic structures that have several electron and hole bands. In multiband systems, the thermoelectric power S is the sum of the weighted thermoelectric contribution of each FS:

$$S = \frac{\Sigma \alpha_n}{\Sigma \sigma_n} = \frac{\Sigma \sigma_n S_n}{\Sigma \sigma_n} \approx \frac{\sigma_e S_e + \sigma_h S_h}{\sigma_e + \sigma_h}, \quad (1)$$

where the Peltier conductivity $\alpha_n = \sigma_n S_n$ of a band with index n is determined by the band-specific thermoelectric power S_n and electrical conductivity σ_n. Multiband conduction can be approximated by a two-band conduction model with dominant electron (e) and hole (h) bands. In this model, the sign changes of $S(T)$ across the phase transitions of IrTe$_2$ originate from the changes in the dominant carrier type.

To study the multiband effect, we measured the magnetic field-dependent Hall resistivity $\rho_{xy}(H)$ at high and low temperatures, as shown in the top and bottom panels of Figs. 3(a) and 3(b), respectively. At high temperatures above T_1, $\rho_{xy}(H)$ linearly depends on the magnetic field with a positive slope for both S1 and S2. This behavior is consistent with the positive $S(T)$ [Figs. 2(a) and 2(c)], indicating dominant hole carriers in the high-temperature normal phase. Below T_1, $\rho_{xy}(H)$ of both samples is nonlinear in field, which is a hallmark of multiband conduction. The detailed field dependencies of $\rho_{xy}(H)$ differ significantly from each other. To present the nonlinearity of $\rho_{xy}(H)$ more clearly, we plot the difference $\Delta\rho_{xy}(H) = \rho_{xy}(H) - R_H H$ in the insets of Figs. 3(a) and 3(b), where the Hall coefficient R_H can be determined using the slope of $\rho_{xy}(H)$ [$R_H = d\rho_{xy}(H)/dH$] at low magnetic fields. The nonlinearity of $\rho_{xy}(H)$ is much weaker in S1 than in S2. In S1, $\Delta\rho_{xy}(H)$ at high magnetic fields deviates upward below T_1 and downwards at lower temperatures. In S2, the upward deviation of $\Delta\rho_{xy}(H)$ at high magnetic fields is observed below T_1 and maintained to low temperatures. Thus, the transport properties of electron and hole carriers are sensitive to stripe-charge patterns in IrTe$_2$.

In the two-band model, the field-dependent Hall resistivity $\rho_{xy}(H)$ is described as follows [41]:

$$\rho_{xy}(H) = \frac{1}{e} \frac{(n_h \mu_h^2 - n_e \mu_e^2) + \mu_h^2 \mu_e^2 H^2 (n_h - n_e)}{(n_h \mu_h + n_e \mu_e)^2 + \mu_h^2 \mu_e^2 H^2 (n_h - n_e)^2} H, \quad (2)$$

where $n_{e(h)}$ and $\mu_{e(h)}$ are the densities and mobilities of electron (hole) carriers, respectively. Using the constraint of the
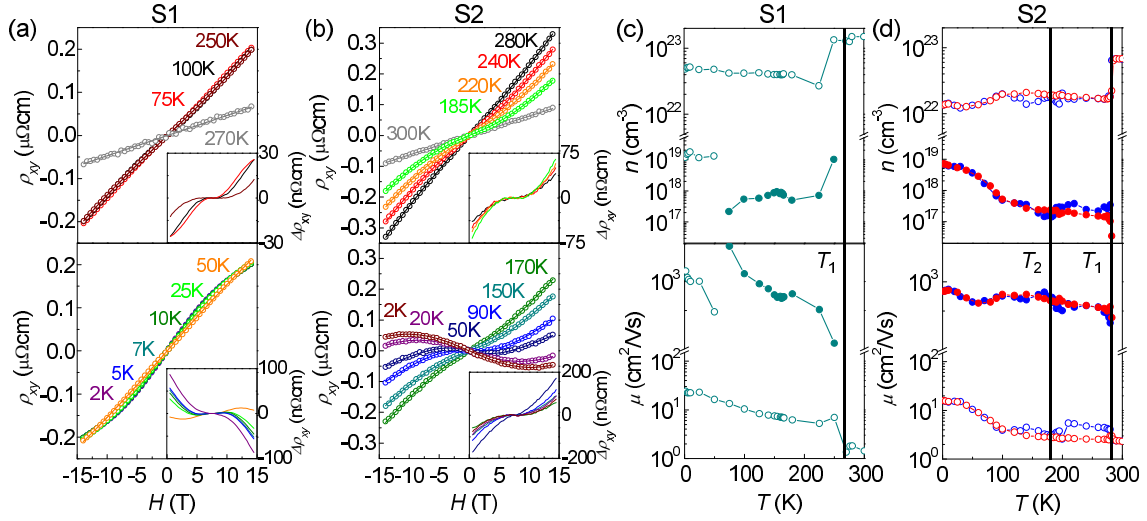
FIG. 3. Magnetic field dependent Hall resistivities ρ_{xy} of (a) S1 and (b) S2 at different temperatures. The fit to the two-band model [Eq. (2)] is shown with solid lines. The insets show the deviation of the Hall resistivity $\Delta\rho_{xy}(H)$ from the low-field linear dependence. Densities n and mobilities μ of electron (solid symbol) and hole (open symbols) carriers for (c) S1 and (d) S2, estimated from the fit shown in (a) and (b), respectively. The blue (red) symbols in (d) correspond to the data taken during cooling (warming). The vertical lines in (c) and (d) indicate the transition temperatures T_1 and T_2 for the stripe-charge orders.

zero-field resistivity [Figs. 1(g) and 1(h)] described by $\rho^{-1} = n_e e \mu_e + n_h e \mu_h$, we fitted the $\rho_{xy}(H)$ curves, which yields $n_{e,h}$ and $\mu_{e,h}$ as a function of temperature [Figs. 3(c) and 3(d)]. When the temperature decreases below T_1, the electron carrier density n_e suddenly appears, whereas n_h decreases in both samples. These trends are consistent with the FS reconstruction due to the stripe order of $5a_0$. In the previous ARPES measurements [19] above and below T_1, it has been shown that the charge transfer from Ir^{3+} to Te_2^{3-} due to dimerization introduces additional electrons in the Te $5p$ band below T_1. The additional electrons with a density n_e, lower than n_h, are much more mobile than holes ($\mu_e > \mu_h$). However, the conductivity of electrons $n_e e \mu_e$ is still lower than that of holes $n_h e \mu_h$, and hole carriers are dominant even below T_1, thereby maintaining a positive R_H (Fig. 3). This observation seems inconsistent with the observed negative S below T_1.

Regarding the transition between two stripe phases of $5a_0$ and $8a_0$ at T_2 in S2, the two-band model also cannot explain the sign change of $S(T)$. Unlike the transition at T_1, n_h and n_e change mildly across T_2 [Fig. 3(d)]. With lowering temperature across T_2, μ_h decreases sharply, while μ_e remains approximately constant [Fig. 3(d)]. According to the two-band model [Eq. (1)], the decrease in μ_h implies a decrease of $S(T)$, under the assumption that S_h and S_e do not change drastically during the transition. However, in experiments, $S(T)$ increases from negative to positive across T_2 [Fig. 2(c)]. Therefore, identifying the dominant carrier type based on the Hall effect measurements is insufficient for understanding the complex sign changes in $S(T)$ across the transitions in $IrTe_2$. Instead, the substantial changes in the contribution of each band to the total S must be considered in the stripe-charge ordering phases.

To examine the band-specific contribution to the total S in the different stripe phases, we calculated FSs of the high-temperature normal and the low-temperature stripe phases with $5a_0$ and $8a_0$. The calculated FSs are consistent with those presented in previous reports, which are in good agreement with dHvA oscillations and ARPES results [26,27,32]. Figure 4 displays the reconstructed FSs of the stripe phases with $5a_0$ and $8a_0$, showing multiple quasi-two-dimensional pockets with different Fermi velocities v_F. In both $5a_0$ and $8a_0$ phases, the bands are folded according to the periodicity of the dimer patterns, and the hole FSs of the normal phase [18,19,32,40] are reconstructed into several electron and hole FSs [42] [Figs. 4(a) and 4(b)]. The small FS pockets, centered at the A point of the first Brillouin zone, were identified as electron type with high v_F, whereas the FSs centered at the Γ point are hole type with low v_F. These high-v_F electrons and low-v_F holes contribute to multiband conduction, in good agreement with the Hall resistivity results [Figs. 3(c) and 3(d)].

Using these calculated FSs of the normal and stripe phases with $5a_0$ and $8a_0$, the electric conductivity σ_n and Peltier conductivity α_n (n is the band index) were estimated by the Boltzmann transport calculations with a constant scattering time. For the stripe phases, the calculated Peltier conductivities $\alpha_{i,n}$ and $\alpha_{j,n}$, parallel (i) and perpendicular (j) to the stripe direction within the $IrTe_2$ layer, were averaged out by assuming a homogeneous population of the stripe domains, i.e., $\alpha_n \simeq (\alpha_{i,n} + \alpha_{j,n})/2$. Note that $\alpha_{i,n}$ and $\alpha_{j,n}$ are different for a given stripe phase, which reflects the anisotropy of the stripe-charge order. Detailed features of this anisotropy are presented in Figs. 6 and 7 in the Appendix. As ρ_{xy} is much smaller than ρ_{xx}, as shown in Fig. 3 ($\sigma_{xy} \ll \sigma_{xx}$), and $S_{xy} \ll S_{xx}$ were assumed owing to the Sondheimer cancellation, $\alpha_{i,n}$ and $\alpha_{j,n}$ were determined with the diagonal components of the calculated $S_{ij,n}$ and $\sigma_{ij,n}$ tensors for each band, i.e., $\alpha_{i,n} = \sigma_{ii,n}S_{ii,n} + \sigma_{ij,n}S_{ji,n} \simeq \sigma_{ii,n}S_{ii,n}$ and, similarly, $\alpha_{j,n} \simeq \sigma_{jj,n}S_{jj,n}$. Once the band-specific Peltier conductivities α_n for the multiple FSs in the $5a_0$ or $8a_0$ phases are calculated, they were compared with α_n of the hypothetical
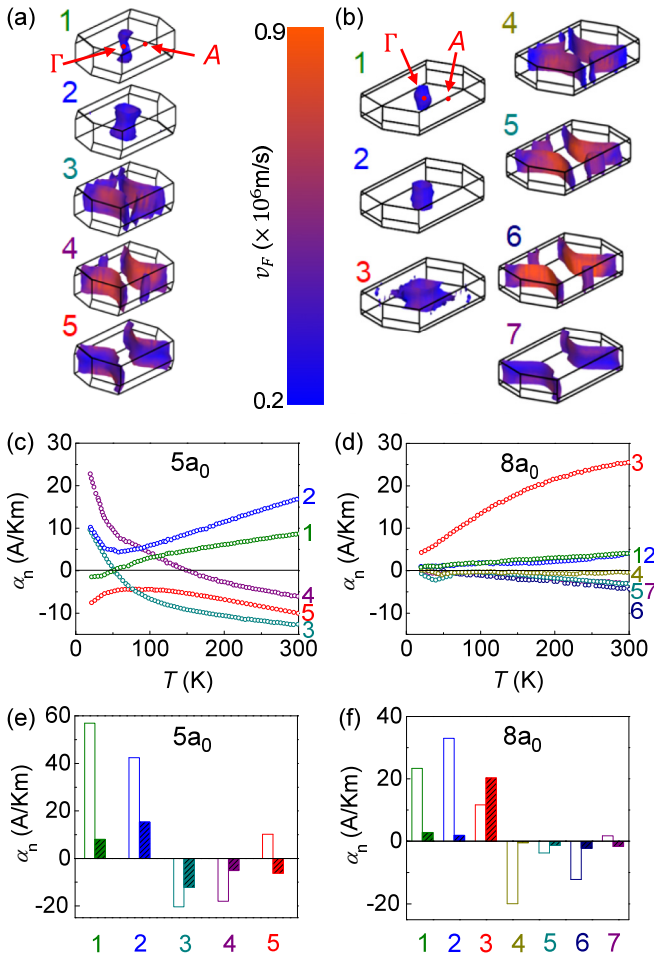
FIG. 4. Reconstructed Fermi surfaces and Fermi velocities v_F of IrTe$_2$ in the (a) $5a_0$ and (b) $8a_0$ phases. Calculated Peltier conductivity α_n (n is the band index) for the (c) $5a_0$ and (d) $8a_0$ phases. Calculated α_n at the transition temperatures (e) $T_1 = 270$ K for the $5a_0$ phase and (f) $T_2 = 180$ K for the $8a_0$ phase (filled bars). For comparison, α_n of the corresponding normal phases with unit cell sizes of the $5a_0$ and $8a_0$ phases (unfilled bars) is also shown in (e) and (f).

normal phase, in which the unit cell size is matched to those of the $5a_0$ or $8a_0$ phases but the internal atomic positions are identical to those of the normal phase. In this comparison, we can track the change in α_n with and without stripe-charge orders and identify the FS responsible for the sign change in $S(T)$ at the transition temperatures.

The Peltier conductivity α_n of each FS for the stripe phases with $5a_0$ and $8a_0$ is shown in Figs. 4(c) and 4(d). Each FS contributes with different signs to the total $S(T)$, the sign of which is determined by the balance of these contributions. The comparison of the band-specific α_n values for the normal, $5a_0$, and $8a_0$ phases reveals the FSs responsible for the sign change of $S(T)$. We found that at $T_1 \sim 270$ K, α_n of the hole FSs ($n = 1, 2$) is significantly reduced in the $5a_0$ phase, compared to the value of the normal phase [Fig. 4(e)]. In addition, α_n's sign of the open FS ($n = 5$) changes from positive to negative owing to the stripe order. These FSs ($n = 1, 2, 5$) are
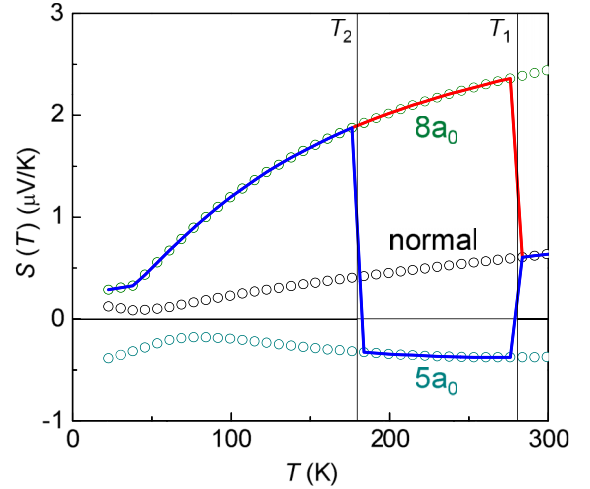

FIG. 5. Calculated thermoelectric power $S(T)$ for the normal and stripe-charge ordering phases with $5a_0$ and $8a_0$ modulation patterns. The blue and red solid curves represent the expected $S(T)$ curve for S2 during cooling and warming, respectively.

responsible for the sign change in $S(T)$ across the transition from the normal to the $5a_0$ phase. Similarly, in the $8a_0$ phase at $T_2 \sim 180$ K, all the FSs have a small α_n, except the hole FS ($n = 3$), as shown in Fig. 4(f). This FS has a large positive contribution, which dominates over those of the other FSs. This dominance explains the change in $S(T)$ to a positive sign in the $8a_0$ phase. These results demonstrate that the subtle balance between the positive and negative contributions of the multiple FSs determines the total $S(T)$, which highly depends on the FS reconstruction.

When the contributions from multiple FSs are added up using Eq. (1), the calculated $S(T)$ is negative in the $5a_0$ phase and positive in the $8a_0$ phases (Fig. 5). These results can be compared with $S(T)$ of the normal phase, which was estimated using $S(T) = \alpha(T)/\sigma(T)$ from the calculated Peltier [$\alpha(T)$] and electrical [$\sigma(T)$] conductivities for a hole FS in the normal phase [32]. We found that the calculated $S(T)$ curves correctly reproduce the experimentally observed sign changes in $S(T)$ across the transitions [Figs. 2(a) and 2(c)], except the low-temperature hump due to the phonon drag effect, which is not included in the Boltzmann transport calculations. This agreement suggests that the substantial changes in the thermoelectric contribution of each FS are induced by the stripe-order-driven FS reconstruction. Therefore, these results confirm FS reconstruction in the stripe-charge ordering phases and its drastic effect on the intrinsic charge conduction in IrTe$_2$.

IV. CONCLUSION

In conclusion, using high-quality IrTe$_2$ crystals with a single phase transition to the $5a_0$ phase or successive stripe transitions to the $5a_0$ and $8a_0$ phases, we investigated the electrical and thermal transport properties across the stripe phase transitions. While the abrupt anomalies in the resistivity and thermal conductivity are mostly determined by domain

boundary scattering, the Hall effect and thermoelectric power $S(T)$ reflect the multiband nature in the stripe phases. In particular, the complex sign changes in $S(T)$ in the different stripe phases can be well explained by FS reconstruction due to the stripe orders with a cross-layer quasi-two-dimensionality. This intriguing charge ordered phase in the metallic state significantly modifies the electrical properties, which can also affect the superconductivity coexisting with the charge ordered phase [10–13,21–23,43].

APPENDIX

In this Appendix, we present the Peltier conductivities, $\alpha_{i,n}$ and $\alpha_{j,n}$, parallel (i) and perpendicular (j) to the stripe direction within the IrTe$_2$ layer, respectively. For comparison

we plot the averaged α_n as shown in Fig. 4. In the normal phase, FSs with $n = 1, 2$ have dominant positive contributions to $\alpha_{i,n}$ and $\alpha_{j,n}$, which results in a positive averaged α_n (Fig. 6). These positive contributions to $\alpha_{i,n}$ and $\alpha_{j,n}$ are significantly suppressed in the $5a_0$ phase. Moreover, the positive contribution of the FS with $n = 5$ in the normal phase becomes negative in the $5a_0$ phase for $\alpha_{i,n}$ [Figs. 6(a) and 6(d)]. For $\alpha_{j,n}$, the negative contribution of the FS with $n = 3$ is dominant in the $5a_0$ phase [Figs. 6(b) and 6(e)]. Although the negative contributions of $\alpha_{i,n}$ and $\alpha_{j,n}$ from the FSs with $n = 3, 4$ are somewhat reduced in magnitude by the stripe transition with $5a_0$, the strong reduction in $\alpha_{i,n}$ of the FSs with $n = 1, 2, 5$ and $\alpha_{j,n}$ of the FSs with $n = 1, 2$, is dominant. This leads to the change in $S(T)$ from a positive to a negative sign at $T_1 \sim 270$ K [Figs. 2(a) and 2(c)].

The same analysis was performed on the $8a_0$ phase, as shown in Fig. 7. In the normal phase, the positive contributions to $\alpha_{i,n}$ and $\alpha_{j,n}$ from the FSs with $n = 1, 2, 3$ dominate over the negative contributions to $\alpha_{j,n}$ of the FSs with $n = 4, 5, 6$. This results in a positive S of the normal phase at $T_2 \sim 180$ K, consistent with the calculation above. Meanwhile, in the $8a_0$ phase, the contributions to $\alpha_{i,n}$ and $\alpha_{j,n}$ from all the FSs become much smaller than those of the normal phase, except that of the FS with $n = 3$ (Fig. 7). For the FS with $n = 3$, $\alpha_{i,n}$ and $\alpha_{j,n}$ are increased due to the $8a_0$ order [Figs. 7(d) and 7(e)], which increases S at $T_2 \sim 180$ K. Therefore, the transition from the $5a_0$ phase to the $8a_0$ phase at T_2 during cooling leads to the change in $S(T)$ from a negative to a positive sign. This is consistent with experimental results [Fig. 2(c)].
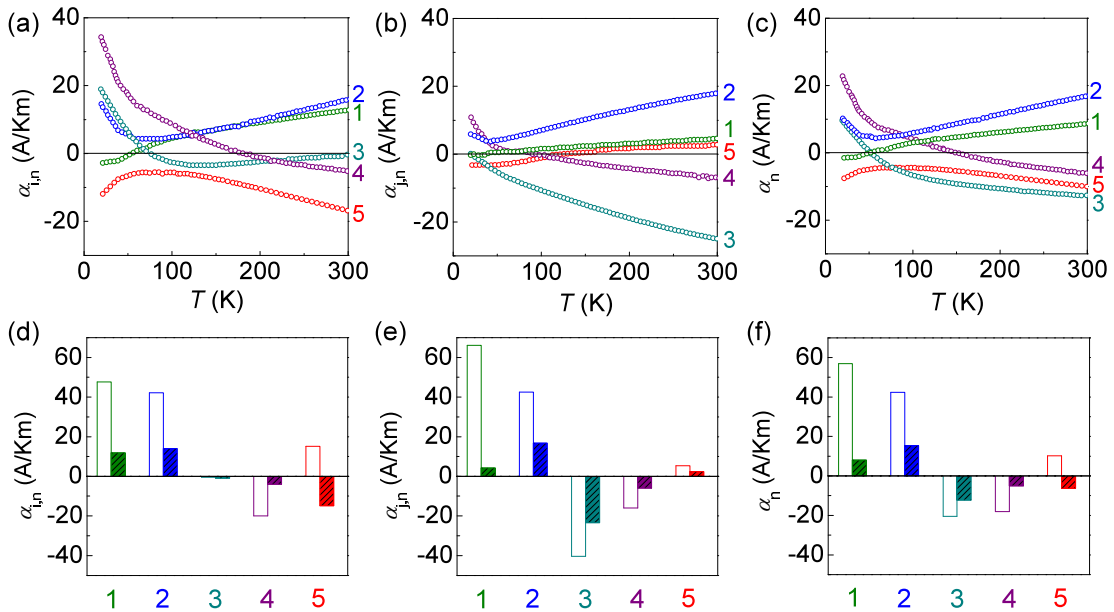

FIG. 6. Calculated Peltier conductivities (a) $\alpha_{i,n}$, (b) $\alpha_{j,n}$, and (c) the averaged α_n as a function of temperature for the $5a_0$ phase. The band index n corresponds to the same index as in Fig. 4(a). The indices i and j indicate the components parallel and perpendicular to the stripe direction within the IrTe$_2$ layer, respectively. Peltier conductivities of the $5a_0$ phase (filled bars) and normal phase (unfilled bars) for (d) $\alpha_{i,n}$, (e) $\alpha_{j,n}$, and (f) the averaged α_n at the transition temperature $T_1 \sim 270$ K.
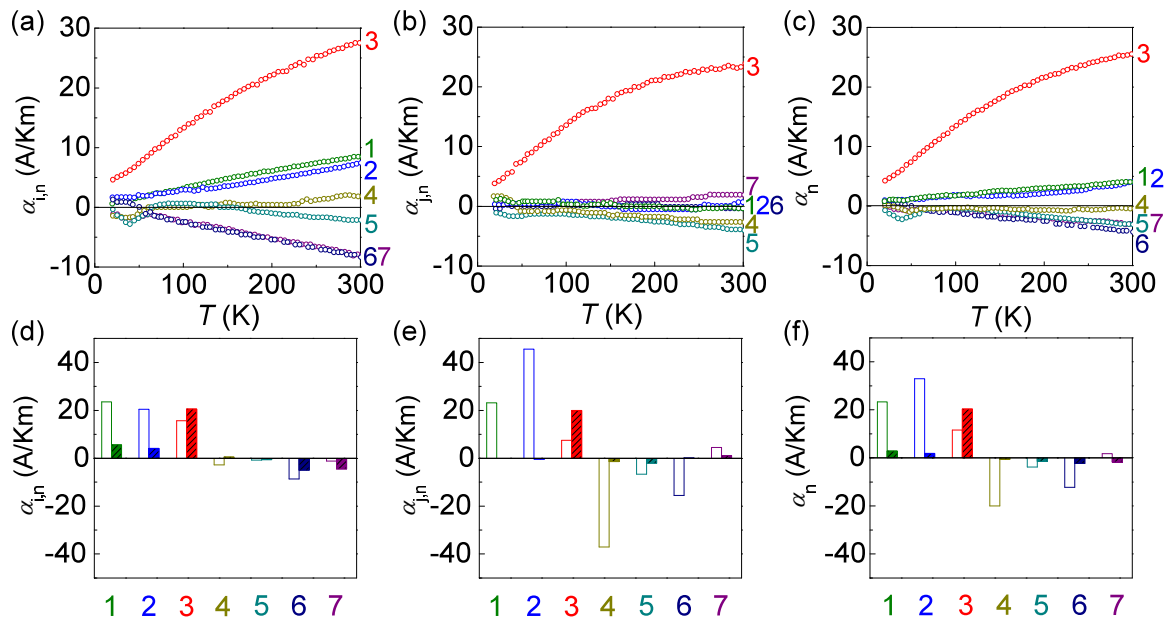
FIG. 7. Calculated Peltier conductivities (a) $\alpha_{i,n}$, (b) $\alpha_{j,n}$, and (c) the averaged α_n as a function of temperature for the $8a_0$ phase. The band index n corresponds to the same index as Fig. 4(b). The indices i and j indicate the components parallel and perpendicular to the stripe direction within the IrTe$_2$ layer, respectively. Peltier conductivities of the $8a_0$ phase (filled bars) and normal phase (unfilled bars) for (d) $\alpha_{i,n}$, (e) $\alpha_{j,n}$, and (f) the averaged α_n at the transition temperature $T_2 \sim 180$ K.

[1] D. E. Moncton, J. D. Axe, and F. J. DiSalvo, Phys. Rev. Lett. **34**, 734 (1975).

[2] X. L. Wu and C. M. Lieber, Science **243**, 1703 (1989).

[3] Th. Straub, Th. Finteis, R. Claessen, P. Steiner, S. Hufner, P. Blaha, C. S. Oglesby, and E. Bucher, Phys. Rev. Lett. **82**, 4504 (1999).

[4] H. Cercellier, C. Monney, F. Clerc, C. Battaglia, L. Despont, M. G. Garnier, H. Beck, P. Aebi, L. Patthey, H. Berger, and L. Forro, Phys. Rev. Lett. **99**, 146403 (2007).

[5] B. Sipos, A. F. Kusmartseva, A. Akrap, H. Berger, L. Forro, and E. Tutis, Nat. Mater. **7**, 960 (2008).

[6] A. Splendiani, L. Sun, Y. Zhang, T. Li, J. Kim, C.-Y. Chim, G. Galli, and F. Wang, Nano Lett. **10**, 1271 (2010).

[7] X. Wang, Y. Gong, G. Shi, L. Chow, K. Keyshar, G. Ye, R. Vajtai, J. Lou, Z. Liu, E. Ringe, B. K. Tay, and P. M. Ajayan, ACS Nano **8**, 5125 (2014).

[8] S. Yan, D. Iaia, E. Morosan, E. Fradkin, P. Abbamonte, and V. Madhavan, Phys. Rev. Lett. **118**, 106405 (2017).

[9] S. Manzeli, D. Ovchinnikov, D. Pasquier, O. V. Yazyev, and A. Kis, Nat. Rev. Mater. **2**, 17033 (2017).

[10] J. J. Yang, Y. J. Choi, Y. S. Oh, A. Hogan, Y. Horibe, K. Kim, B. I. Min, and S.-W. Cheong, Phys. Rev. Lett. **108**, 116402 (2012).

[11] S. Pyon, K. Kudo, and M. Nohara, J. Phys. Soc. Jpn. **81**, 053701 (2012).

[12] A. F. Fang, G. Xu, T. Dong, P. Zheng, and N. L. Wang, Sci. Rep. **3**, 1153 (2013).

[13] A. Kiswandhi, J. S. Brooks, H. B. Cao, J. Q. Yan, D. Mandrus, Z. Jiang, and H. D. Zhou, Phys. Rev. B **87**, 121107(R) (2013).

[14] Y. S. Oh, J. J. Yang, Y. Horibe, and S.-W. Cheong, Phys. Rev. Lett. **110**, 127209 (2013).

[15] H. Cao, B. C. Chakoumakos, X. Chen, J. Yan, M. A. McGuire, H. Yang, R. Custelcean, H. Zhou, D. J. Singh, and D. Mandrus, Phys. Rev. B **88**, 115122 (2013).

[16] T. Toriyama, M. Kobori, T. Konishi, Y. Ohta, K. Sugimoto, J. Kim, A. Fujiwara, S. Pyon, K. Kudo, and M. Nohara, J. Phys. Soc. Jpn. **83**, 033701 (2014).

[17] Q. Li, W. Lin, J. Yan, X. Chen, A. G. Gianfrancesco, D. J. Singh, D. Mandrus, S. V. Kalinin, and M. Pan, Nat. Commun. **5**, 5358 (2014).

[18] D. Ootsuki, S. Pyon, K. Kudo, M. Nohara, M. Horio, T. Yoshida, A. Fujimori, M. Arita, H. Anzai, H. Namatame, M. Taniguchi, N. L. Saini, and T. Mizokawa, J. Phys. Soc. Jpn. **82**, 093704 (2013).

[19] K. T. Ko, H. H. Lee, D. H. Kim, J. J. Yang, S. W. Cheong, M. J. Eom, J. S. Kim, R. Gammag, K. S. Kim, H. S. Kim, T.-H. Kim, H. W. Yeom, T. Y. Koo, H. D. Kim, and J.-H. Park, Nat. Commun. **6**, 7342 (2015).

[20] H. S. Kim, T.-H. Kim, J. J. Yang, S.-W. Cheong, and H. W. Yeom, Phys. Rev. B **90**, 201103(R) (2014).

[21] M. Kamitani, M. S. Bahramy, R. Arita, S. Seki, T. Arima, Y. Tokura, and S. Ishiwata, Phys. Rev. B **87**, 180501(R) (2013).

[22] O. Ivashko, L. Yang, E. Martino, Y. Chen, C. Y. Guo, H. Q. Yuan, A. Pisoni, P. Matus, S. Pyon, K. Kudo, M. Nohara, L. Forro, H. M. Ronnow, M. Hucker, M. v. Zimmermann, and J. Chang, Sci. Rep. **7**, 17157 (2017).

[23] Y. Liu, H. Lei, K. Wang, M. Abeykoon, J. B. Warren, E. Bozin, and C. Petrovic, Phys. Rev. B **98**, 094519 (2018).

[24] G. Cao, W. Xie, W. A. Phelan, J. F. DiTusa, and R. Jin, Phys. Rev. B **95**, 035148 (2017).

[25] P. J. Hsu, T. Mauerer, M. Vogt, J. J. Yang, Y. S. Oh, S.-W. Cheong, M. Bode, and W. Wu, Phys. Rev. Lett. **111**, 266401 (2013).

[26] M. J. Eom, K. Kim, Y. J. Jo, J. J. Yang, E. S. Choi, B. I. Min, J.-H. Park, S.-W. Cheong, and J. S. Kim, Phys. Rev. Lett. **113**, 266406 (2014).

[27] S. F. Blake, M. D. Watson, A. McCollam, S. Kasahara, R. D. Johnson, A. Narayanan, G. L. Pascut, K. Haule, V. Kiryukhin, T. Yamashita, D. Watanabe, T. Shibauchi, Y. Matsuda, and A. I. Coldea, Phys. Rev. B **91**, 121105(R) (2015).

[28] C. Chen, J. Kim, Y. Yang, G. Cao, R. Jin, and E. W. Plummer, Phys. Rev. B **95**, 094118 (2017).

[29] T. Machida, Y. Fujisawa, K. Igarashi, A. Kaneko, S. Ooi, T. Mochiku, M. Tachiki, K. Komori, K. Hirata, and H. Sakata, Phys. Rev. B **88**, 245125 (2013).

[30] J. Dai, K. Haule, J. J. Yang, Y. S. Oh, S.-W. Cheong, and W. Wu, Phys. Rev. B **90**, 235121 (2014).

[31] G. L. Pascut, K. Haule, M. J. Gutmann, S. A. Barnett, A. Bombardi, S. Artyukhin, T. Birol, D. Vanderbilt, J. J. Yang, S.-W. Cheong, and V. Kiryukhin, Phys. Rev. Lett. **112**, 086402 (2014).

[32] K. Kim, S. Kim, K. T. Ko, H. Lee, J.-H. Park, J. J. Yang, S. W. Cheong, and B. I. Min, Phys. Rev. Lett. **114**, 136401 (2015).

[33] T. Mauerer, M. Vogt, P.-J. Hsu, G. L. Pascut, K. Haule, V. Kiryukhin, J. J. Yang, S.-W. Cheong, W. Wu, and M. Bode, Phys. Rev. B **94**, 014106 (2016).

[34] K. Kim, S. Kim, and B. I. Min, Phys. Rev. B **90**, 195136 (2014).

[35] K. Koepernik and H. Eschrig, Phys. Rev. B **59**, 1743 (1999).

[36] G. Pizzi, D. Volja, B. Kozinsky, M. Fornari, and N. Marzari, Comput. Phys. Commun. **185**, 2311 (2014).

[37] A. A. Mostofi, J. R. Yates, G. Pizzi, Y. S. Lee, I. Souza, D. Vanderbilt, and N. Marzari, Comput. Phys. Commun. **185**, 2309 (2014).

[38] J. M. Siman, *Electrons and Phonons* (Oxford University Press, London, 1962).

[39] R. D. Barnard, *Thermoelectricity in Metals and Alloys* (Taylor and Francis, London, 1972).

[40] H. H. Lee, K. T. Ko, K. Kim, B. G. Park, J. J. Yang, S.-W. Cheong, and J.-H. Park, Europhys. Lett. **120**, 47003 (2017).

[41] R. G. Chambers, Proc. Phys. Soc. London, Ser. A **65**, 903 (1952).

[42] D. Ootsuki, H. Ishii, K. Kudo, M. Nohara, M. Arita, H. Namatame, M. Taniguchi, N. L. Saini, and T. Mizokawa, J. Phys. Chem. Solids **128**, 270 (2019).

[43] S. Park, S. Y. Kim, H. K. Kim, M. J. Kim, H. Kim, G. S. Choi, C. J. Won, S. Kim, K. Kim, E. F. Talantsev, K. Watanabe, T. Taniguchi, S.-W. Cheong, B. J. Kim, H. W. Yeom, J. Kim, T.-H. Kim, and J. S. Kim, arXiv:2009.12578.